

## Supporting Information

### **Conductive metal-organic frameworks as ion-to-electron transducers in potentiometric sensors**

Lukasz Mendecki<sup>†</sup> and Katherine A. Mirica<sup>\*,a</sup>

<sup>a</sup> Burke Laboratory, 41 College Street, Dartmouth College, Hanover, NH, USA

Corresponding Authors Email: [Katherine.A.Mirica@dartmouth.edu](mailto:Katherine.A.Mirica@dartmouth.edu)

## Contents

Scanning Electron Microscopy and Energy Dispersive X-Ray Spectroscopy of M <sub>3</sub> HHTP <sub>2</sub>	
Materials .....	S-3
Powder X-ray Diffraction (pXRD) of M <sub>3</sub> HHTP <sub>2</sub> MOFs.....	S-4
X-ray Photoelectron Spectroscopy (XPS) of M <sub>3</sub> HHTP <sub>2</sub> MOFs .....	S-5
Interferometry of GCE/ MOF Electrodes .....	S-9
Interferometry of GCE/Ni <sub>3</sub> HHTP <sub>2</sub> MOF Electrodes .....	S-10
Electrochemical Impedance Spectroscopy of GCE/Ni <sub>3</sub> HHTP <sub>2</sub> MOF at Different Applied Potentials.....	S-13
Potentiometric Responses Obtained for the ISEs Containing M <sub>3</sub> HHTP <sub>2</sub> MOFs as Underlying Conductive Layer.....	S-14
Potentiometric Slopes Obtained for Various Cations and Anions During Selectivity Measurements of Potassium and Nitrate Selective Electrodes.....	S-14
Light Stability of K <sup>+</sup> -ISM-II Electrodes with Drop-cast Layer of Ni <sub>3</sub> HHTP <sub>2</sub> MOF.....	S-18
Powder X-ray Diffraction (pXRD) of M <sub>3</sub> HHTP <sub>2</sub> MOFs After Potentiometric Measurements.....	S-18
Contact Angle of Water on the Surface of Ni <sub>3</sub> HHTP <sub>2</sub> Coated Electrodes. ....	S-19
References .....	S-19

## Scanning Electron Microscopy and Energy Dispersive X-Ray Spectroscopy of $M_3$ HHTP<sub>2</sub> Materials

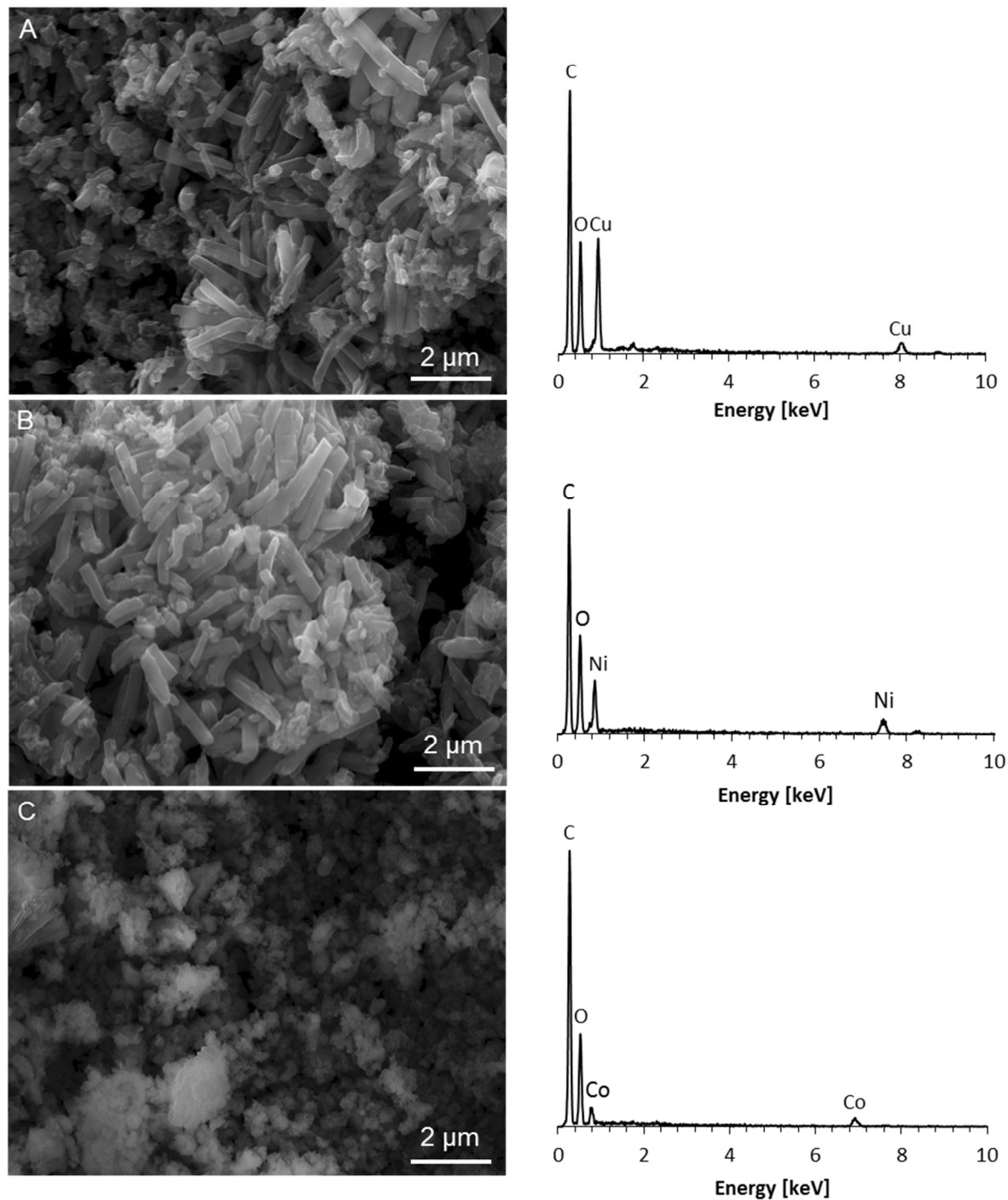


**Figure S1.** SEM results and accompanied EDX analysis collected for the (A)  $Cu_3HHTP_2$  MOF, (B)  $Ni_3HHTP_2$  MOF, and (C)  $Co_3HHTP_2$  MOF. SEM revealed the assembly of  $M_3HHTP_2$  conductive MOFs into nanocrystalline structures while EDX confirmed the presence of organic-inorganic hybrid materials as reported for other HHTP based MOFs.<sup>1</sup>

## Powder X-ray Diffraction (pXRD) of $M_3HHTP_2$ MOFs

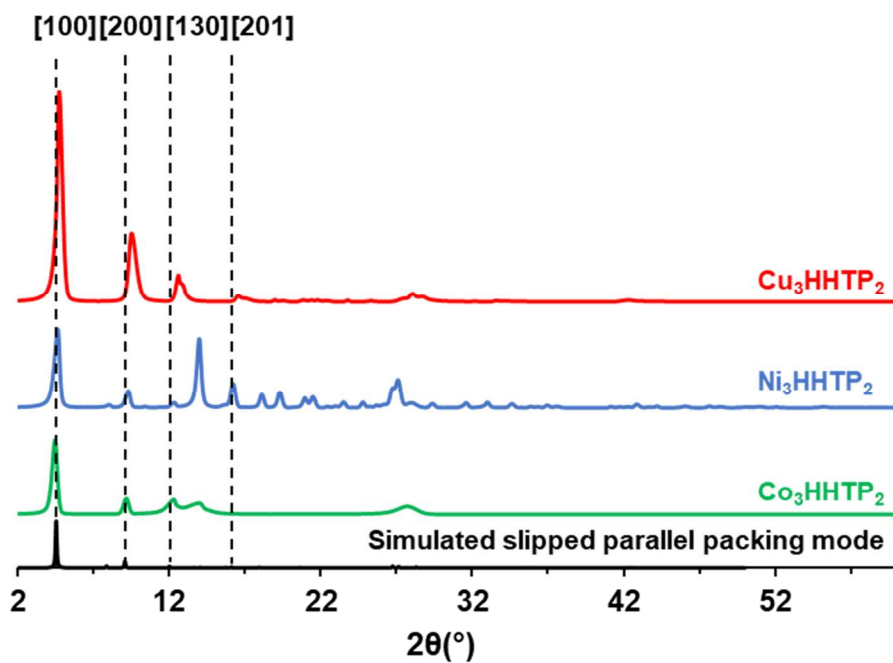


**Figure S2.** Experimental (colored) and simulated slipped parallel powder X-Ray Diffraction patterns without the presence of interpolated layer obtained for bulk  $Cu_3HHTP_2$ ,  $Ni_3HHTP_2$  and  $Co_3HHTP_2$  MOFs. The observed pXRD patterns of  $Cu_3HHTP_2$ ,  $Ni_3HHTP_2$ , and  $Co_3HHTP_2$  MOF are consistent with previous reports.<sup>1,2</sup>

### X-ray Photoelectron Spectroscopy (XPS) of $M_3HHTP_2$ MOFs

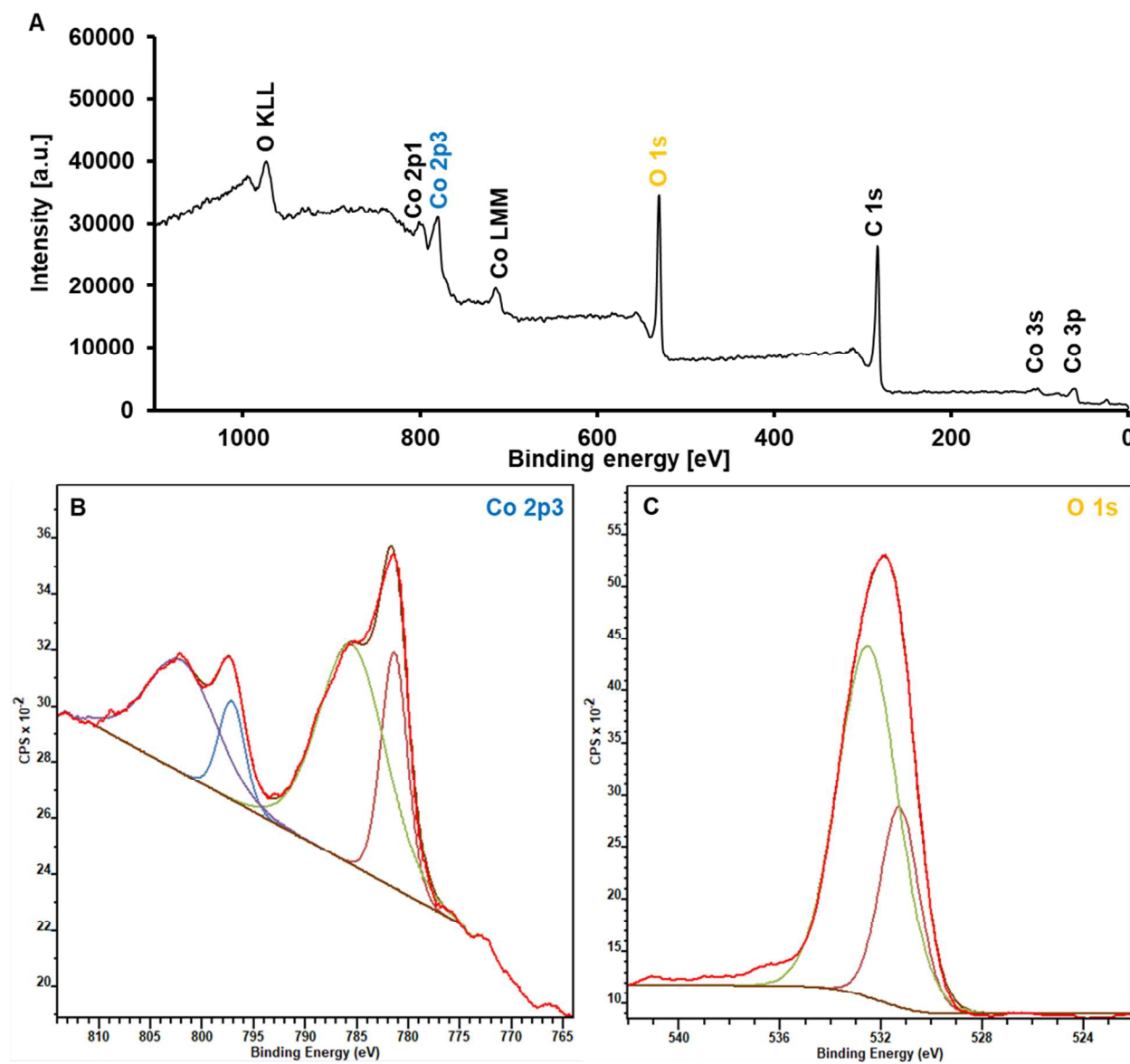


**Figure S3.** XPS spectra obtained for the  $Co_3HHTP_2$  MOFs. (A) Energy survey scan. High-resolution spectrum in the O 1s (B), and Co 2p3 (C) regions.

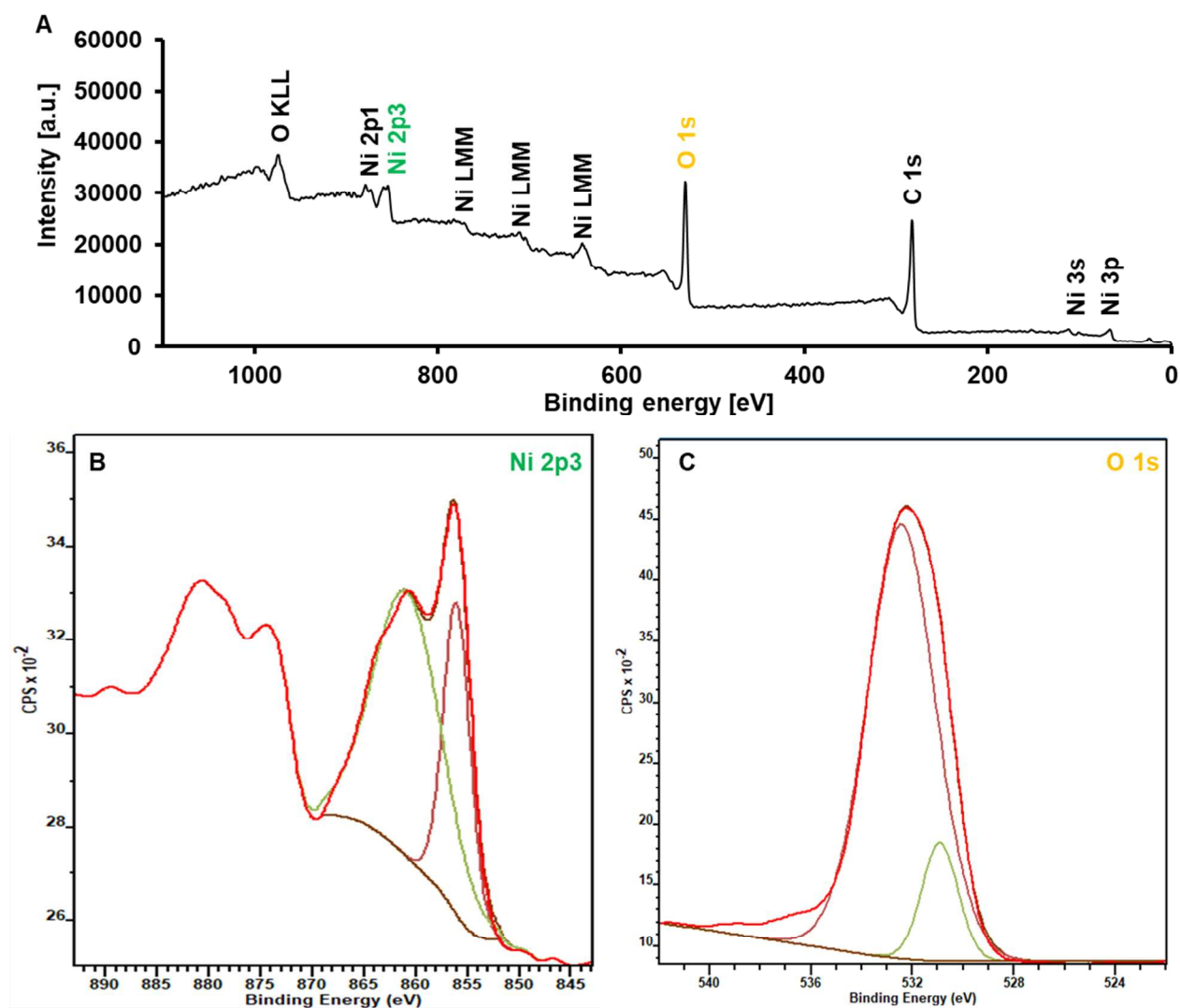


**Figure S4.** XPS spectra obtained for the  $\text{Ni}_3\text{HHTP}_2$  MOFs. (A) Energy survey scan. High-resolution spectrum in the O 1s (B), and Ni 2p<sub>3</sub> (C) regions.

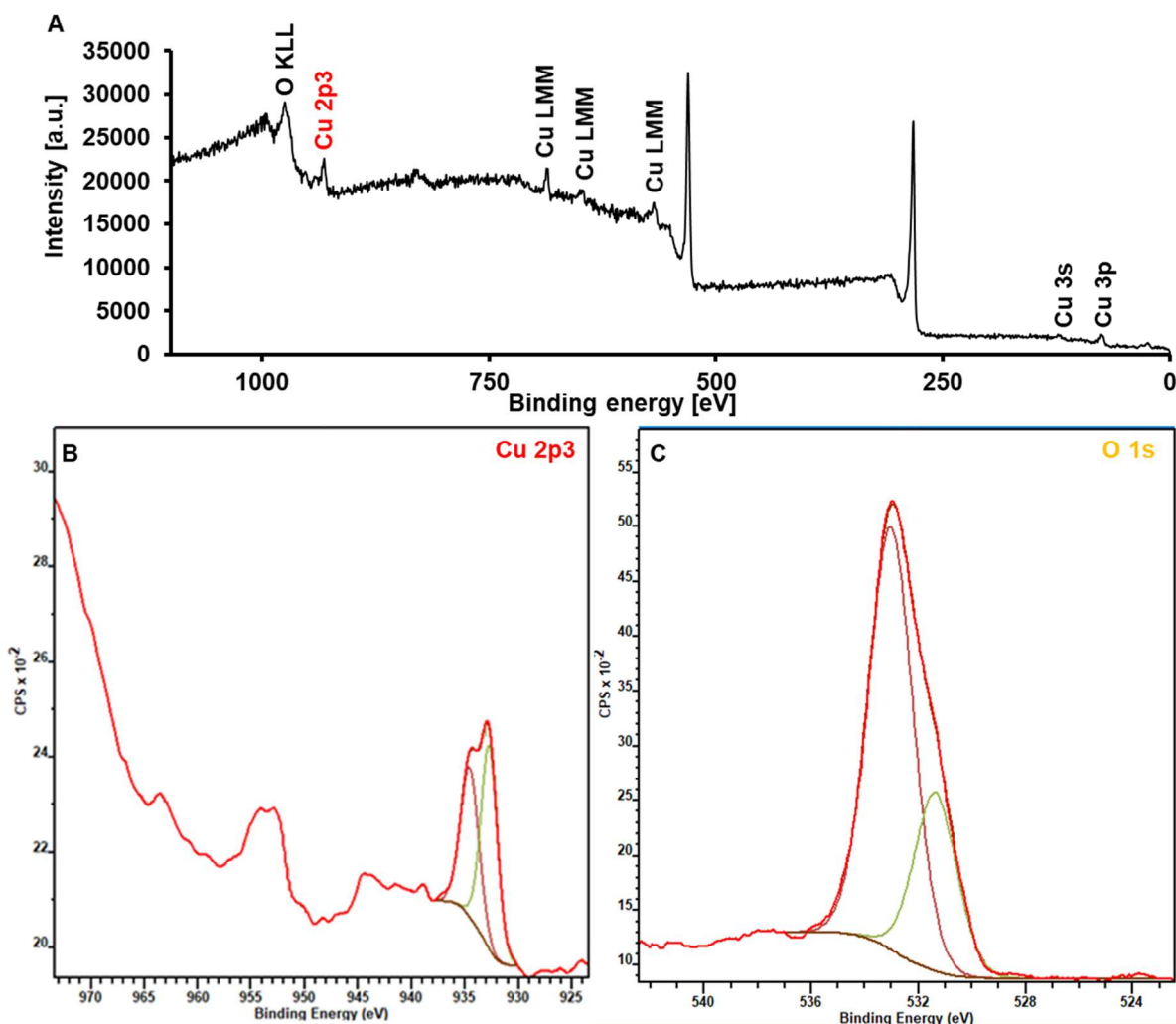


**Figure S5.** XPS spectra obtained for the Cu<sub>3</sub>HHTP<sub>2</sub> MOFs. (A) Energy survey scan. High-resolution spectrum in the O 1s (B), and Cu 2p<sub>3</sub> (C) regions.

The XPS spectra confirmed the presence of O and C along with the respective metals (Co, Cu and Ni) used for the preparation of M<sub>3</sub>HHTP<sub>2</sub> MOFs and revealed that all materials are charge neutral, similarly to other literature reports on the M<sub>3</sub>HITP<sub>2</sub> MOF analogs.<sup>3,4</sup> High-resolution XPS analysis further demonstrated that after washing with water and acetone, no traces of the precursors were detected in the M<sub>3</sub>HHTP<sub>2</sub> MOFs indicating the absence of potentially charge-balancing counter-ions.

In the high-resolution scan of Co 2p<sub>3/2</sub> region, we observed two sets of peaks with binding energies of ~780 and ~795 eV, which describe the 2p<sub>3/2</sub> and 2p<sub>1/2</sub> levels in the theoretically expected 2:1 ratio.<sup>5,6</sup> Further deconvolution of the 2p<sub>3/2</sub> region revealed the presence of four distinct bands: the peaks at 781.4.2 and 794.1 eV were ascribed to Co<sup>II</sup>, while the peaks found at 785.5 and 802.0 eV were assigned to Co<sup>III</sup> (28% of Co<sup>I</sup> and 72% of Co<sup>III</sup>, **Figure S3**). These findings indicate mixed valency in Co<sub>3</sub>HHTP<sub>2</sub> MOFs, which are in good agreement with other studies on the cobalt based MOFs.<sup>5,6</sup> High-resolution XPS analysis of Cu<sub>3</sub>HHTP<sub>2</sub> MOFs also showed the presence of two peaks at 932.8 and 934.6 eV, which can be ascribed to Cu<sup>I</sup> and Cu<sup>II</sup> centers (55% of Cu<sup>I</sup>, and 45% of Cu<sup>II</sup>), respectively, and similarly to Co<sub>3</sub>HHTP<sub>2</sub> MOFs, are indicative of mixed valency within the framework (**Figure S5**).<sup>3,7</sup> The high-resolution scan of the Ni 2p region showed the presence of two peaks with binding energies of ~851 and ~870 eV, were assigned to the 2p<sub>3/2</sub> and 2p<sub>1/2</sub> levels, respectively (**Figure S4**).<sup>8,9</sup> The lack of charge-balancing counterions in the Cu<sub>3</sub>HHTP<sub>2</sub> and Co<sub>3</sub>HHTP<sub>2</sub> MOFs indicates that the variation from the 2+ oxidation state of the metal is compensated by the redox-active HHTP ligands, which are known to be able to accommodate a wide range of redox states. High-resolution spectrum of the Ni 2p region revealed only a single type of Ni, further confirming that no extraneous Ni<sup>2+</sup> ions are present within the analyzed samples. As such species are the only possible cations that could potentially balance a negatively charge material, these finding are thus strongly indicative of charge neutrality within Ni<sub>3</sub>HHTP<sub>2</sub>. Moreover, deconvoluted high resolution spectrum for O 1s revealed the presence of two different environments ~531 eV and ~532 eV, which were assigned to C-O and C=O, respectively. These two distinct types of O are expected for a charge neutral molecule in which the HHTP ligand can adapt semiquinone and quinone structures (**Figure 1**).



## Interferometry of GCE/ MOF Electrodes

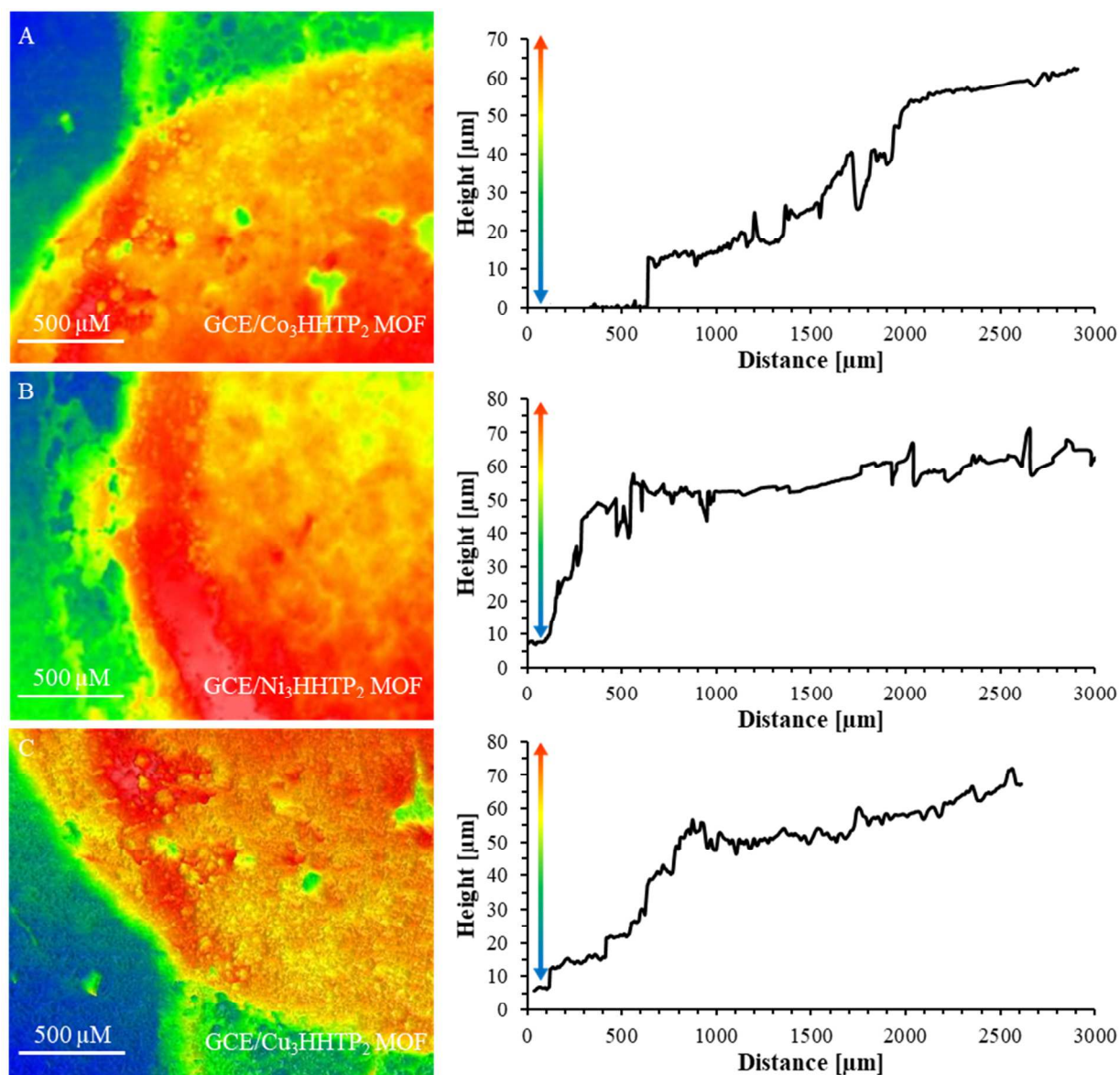


**Figure S6.** Interferometer data for the GCE/ $M_3$ HHTP<sub>2</sub> MOF (M = Co, Ni, Co) electrodes prepared by drop casting 10  $\mu$ L of  $Ni_3$ HHTP<sub>2</sub>-MOF suspension (1 mg/mL) onto top of glassy carbon electrodes. The difference in height between the blue and red regions were used to calculate thickness of the MOF layer.

## Interferometry of GCE/ $\text{Ni}_3\text{HHTP}_2$ MOF Electrodes

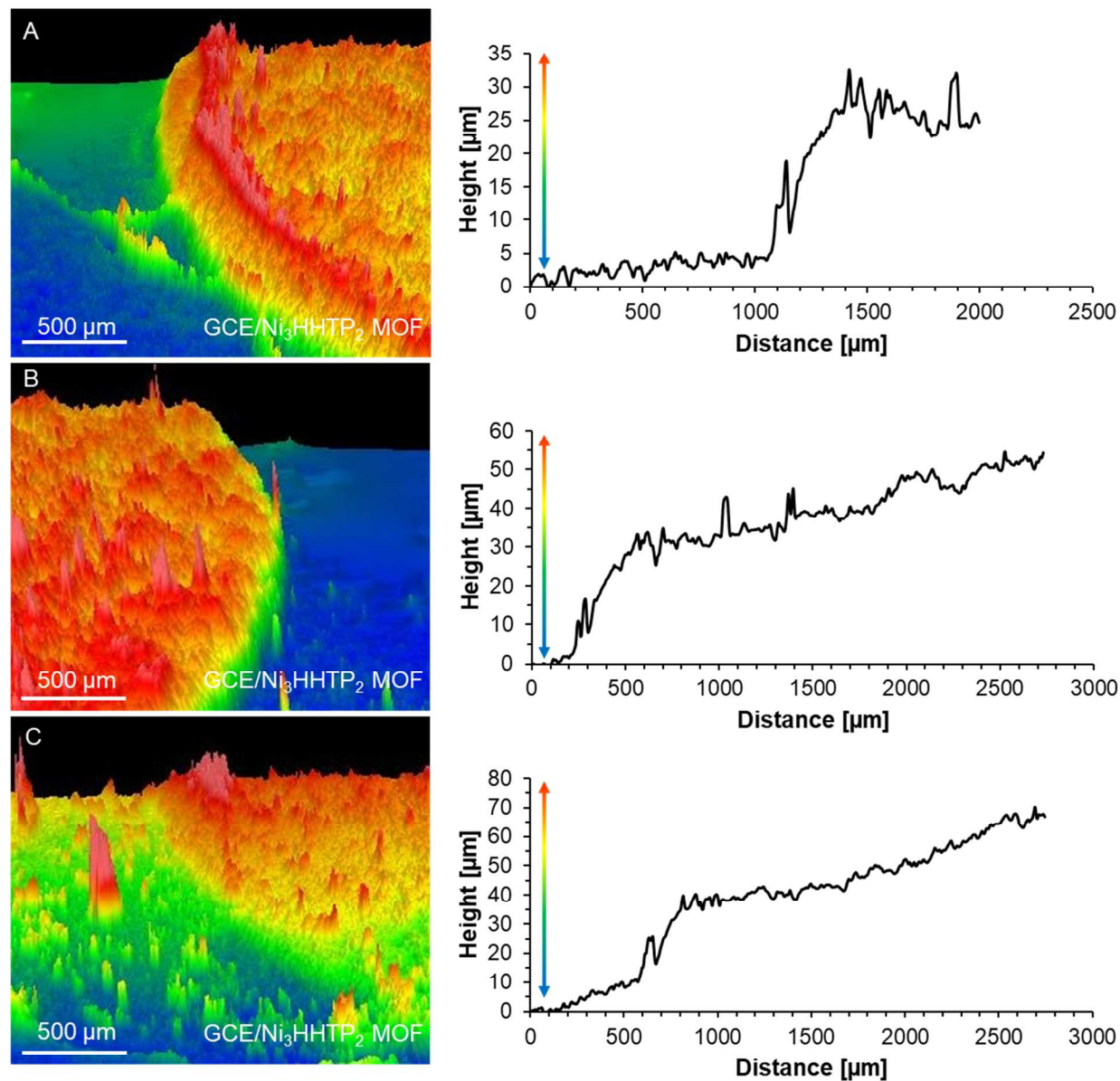


**Figure S7.** Interferometer data for the GCE/MOF electrodes prepared by drop casting A) 2  $\mu\text{L}$ , B) 5  $\mu\text{L}$  and C) 10  $\mu\text{L}$  of  $\text{Ni}_3\text{HHTP}_2$ -MOF suspension (1 mg/mL) onto top of glassy carbon electrodes. The difference in height between the blue and red regions were used to calculate thickness of the MOF layer.

### Cyclic Voltammetry of MOFs Deposited on Glassy Carbon Electrode

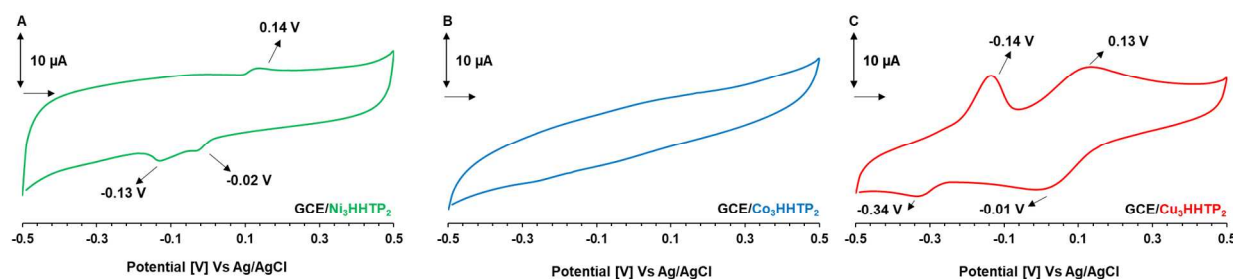


**Figure S8.** Cyclic voltammogram obtained for the glassy carbon electrode coated with 60  $\mu\text{m}$  layer of (A)  $\text{Ni}_3\text{HHTP}_2$ , (B)  $\text{Co}_3\text{HHTP}_2$ , and (C)  $\text{Cu}_3\text{HHTP}_2$  MOFs. Experimental parameters – scan rate: 50 mV/sec, background electrolyte: 0.1 M KCl and scanning range: -0.5 V to 0.5 V. The arrow indicates scan direction.

Electrochemical capacitors can store electrical energy by the i) electrochemical double layer in which charge accumulates at the interface between the electrodes and the electrolyte; or ii) through series of faradic reactions at the surface of electrode materials.<sup>10</sup> Most importantly, in the electrochemical double layer capacitors, there is no electron flow between the solution and the electrode, whereas the interfacial electron transfer between the solution and the electrode, also better known as pseudocapacitance, is observed in the latter example. Therefore, the deliberate introduction of pseudocapacitive components may provide higher capacitance and thus result in more stable potentiometric response.

Cycling voltammetry of  $\text{M}_3\text{HHTP}_2$  MOFs (**Figure S8**) drop-cast onto GCE revealed the presence of one anodic peaks at 0.14 V and two cathodic redox waves at -0.02 V and -0.13 V in  $\text{Ni}_3\text{HHTP}_2$ , and two anodic peaks at -0.14 V and 0.13 V, together with two cathodic redox waves at -0.01 V and -0.34 V indicating the presence of faradic processes in the studied materials. While no faradic reactions were observed for  $\text{GCE/Co}_3\text{HHTP}_2$  electrodes supporting the hypothesis that double layer charging is the primary mechanism responsible for the large capacitance of this material. This observed redox processes recorded for the  $\text{Ni}_3\text{HHTP}_2$  and  $\text{Cu}_3\text{HHTP}_2$  could originate from: i) redox activity of the metal centers or/and ligand within the

MOF network;<sup>11</sup> ii) co-existence of several active redox states due to the presence of defects in the MOF lattice (e.g., exposed-edges);<sup>12</sup> and iii) redox active impurities that are embedded within the coordination network. PXRD and XPS data together (**Figure S2-S5**), demonstrated that no metallic impurities/external species are present within the analyzed  $M_3HHTP_2$  MOFs and thus they are not responsible for the observed redox activity. We hypothesize that the observed redox transformations are due to the redox active nature of the ligand, as reported for the HHTP molecular precursors,<sup>13</sup> which partially contributes to the overall recorded capacitance through the presence of pseudocapacitance. In the case of  $Cu_3HHTP_2$ , the presence of reversible redox waves indicate that the capacitive response of this MOF mainly proceeds through oxidation/reduction of the MOF. In light of these observations, the ion-to-electron transduction process may proceed through i) the formation of the electrical double layer in which one side carries charge in the form of ions, e.g., cations or anions from the ion-selective membrane, while the other side of the capacitor is formed by electrical charge - electrons or holes present in the solid contact; ii) reversible oxidation/reduction (doping/undoping) of the MOF based transducer.

In the former situation, the interfacial potential at the ion selective membrane and MOF interface is solely defined by the quantity of charge stored at the electrical double layer rather than by ion partitioning or redox reactions. Therefore, we anticipate that by using highly porous materials such as  $M_3HHTP_2$  MOFs the interfacial contact between the polymeric membrane and the electrode will be increased giving rise to higher value of capacitance and thus support the hypothesis that signal transduction in  $Ni_3HHTP_2$  and  $Co_3HHTP_2$  mainly proceeds through the formation of electrical double layer as observed for other porous materials. This proposed transduction mechanism may be additionally supported by the XPS and PXRD evidence that revealed charge neutrality in  $M_3HHTP_2$  MOFs and lack of extraneous associated counter-ions

that could potentially participate in the ion-to-electron transduction process through the oxidation/reduction of the MOF based transducer. While, second transduction mechanism may be dominant in the  $\text{Cu}_3\text{HHTP}_2$  MOFs in which reversible redox reaction of the MOF film would ensure stable interfacial potential.

### Electrochemical Impedance Spectroscopy of GCE/ $\text{Ni}_3\text{HHTP}_2$ MOF at Different Applied Potentials

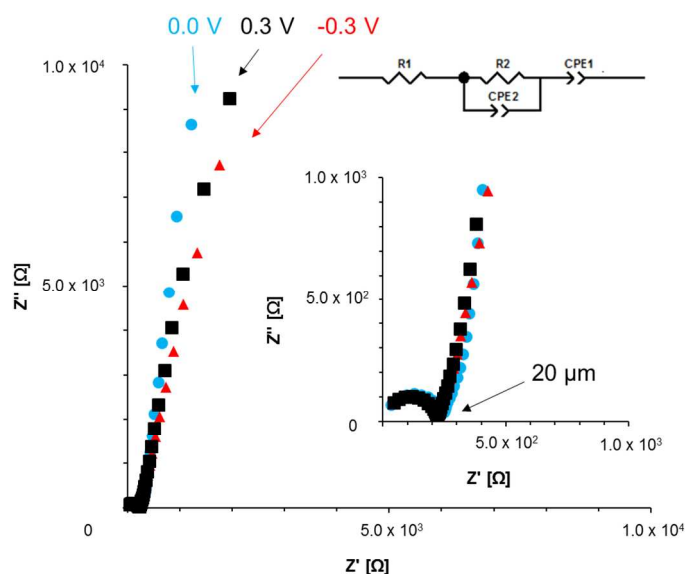


**Figure S9.** (Left) Impedance spectrum obtained for the electrodes at three different applied potentials (0.0 V – blue circles; 0.3 V – black squares; and -0.3 V red triangles) with drop cast  $\text{Ni}_3\text{HHTP}_2$  MOF layer (2  $\mu\text{L}$  aliquot of MOF solution - 20  $\mu\text{m}$  thickness). (Right) Zoomed in representation of the high frequency impedance data for the same electrode configuration (100 kHz – 3 Hz). No significant difference in response characteristics was observed for the studied electrodes. This demonstrates that the total capacitance of the system is independent of the faradic process observed during cyclic voltammetry measurements. Frequency range: 100 kHz – 10 mHz; amplitude potential: 0.01 V; solution: 0.1 M KCl.

### Potentiometric Responses Obtained for the ISEs Containing M<sub>3</sub>HHTP<sub>2</sub> MOFs as Underlying Conductive Layer.

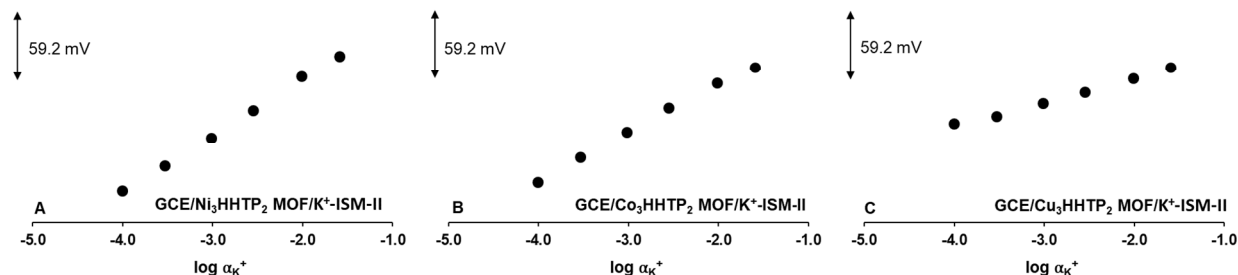


**Figure S10.** Potentiometric responses of M<sub>3</sub>HHTP<sub>2</sub> based ISE for K<sup>+</sup>-ISM-II. In this electrode configuration, either Ni<sub>3</sub>HHTP<sub>2</sub> (A), Co<sub>3</sub>HHTP<sub>2</sub> (B) or Cu<sub>3</sub>HHTP<sub>2</sub> (C) 10  $\mu$ L of Ni<sub>3</sub>HHTP<sub>2</sub>-MOF suspension was drop cast directly onto the glassy carbon electrode and then the resulting conductive layer was covered with potassium selective polymeric membrane (10  $\mu$ L of the K<sup>+</sup>-ISM-II membrane solution as described in the ‘Preparation of K<sup>+</sup> and NO<sub>3</sub><sup>-</sup> sensing membranes’). The slopes obtained for the Ni<sub>3</sub>HHTP<sub>2</sub> MOF/K<sup>+</sup>-ISM-II, Co<sub>3</sub>HHTP<sub>2</sub> MOF/K<sup>+</sup>-ISM-II, and Cu<sub>3</sub>HHTP<sub>2</sub> MOF/K<sup>+</sup>-ISM-II were  $55.1 \pm 1.2$  mV/decade,  $56.2 \pm 1.0$  mV/decade and  $52.6 \pm 2.1$  mV/decade, respectively.

### Potentiometric Slopes Obtained for Various Cations and Anions During Selectivity Measurements of Potassium and Nitrate Selective Electrodes.

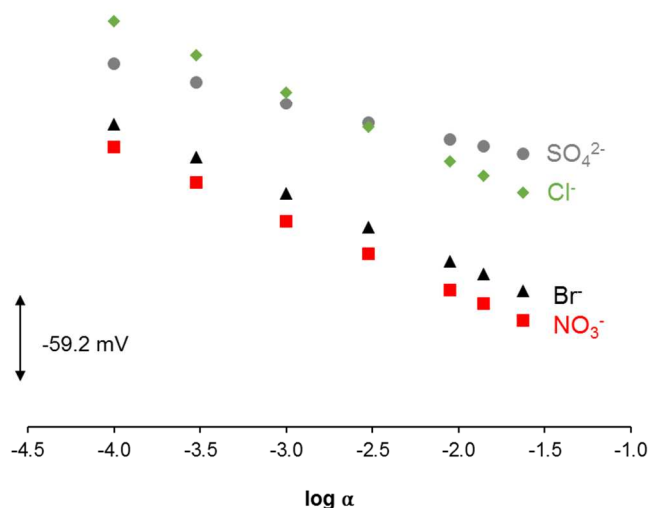


**Figure S11.** Potentiometric responses of glassy carbon electrodes coated with Ni<sub>3</sub>HHTP<sub>2</sub> and then covered with the NO<sub>3</sub><sup>-</sup>-ISM for various cations: Cl<sup>-</sup> (green diamonds), NO<sub>3</sub><sup>-</sup> (red squares), Br<sup>-</sup> (black triangles) and SO<sub>4</sub><sup>2-</sup> (grey circles).

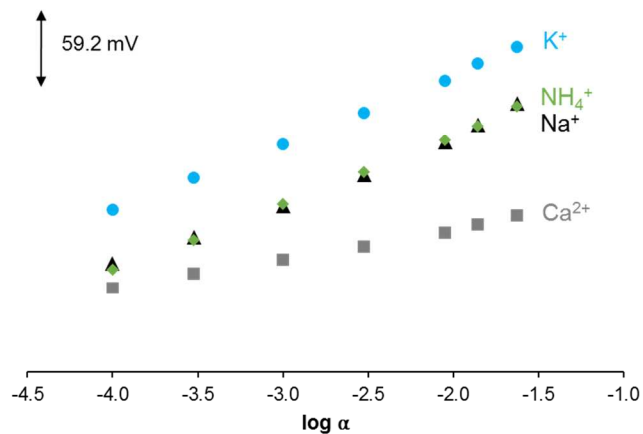


**Figure S12.** Potentiometric responses of glassy carbon electrodes coated with  $\text{Ni}_3\text{HHTP}_2$  and then covered with the  $\text{K}^+$ -ISM-II for various cations:  $\text{K}^+$  (blue circles),  $\text{NH}_4^+$  (green diamonds),  $\text{Na}^+$  (black triangles) and  $\text{Ca}^{2+}$  (grey squares).

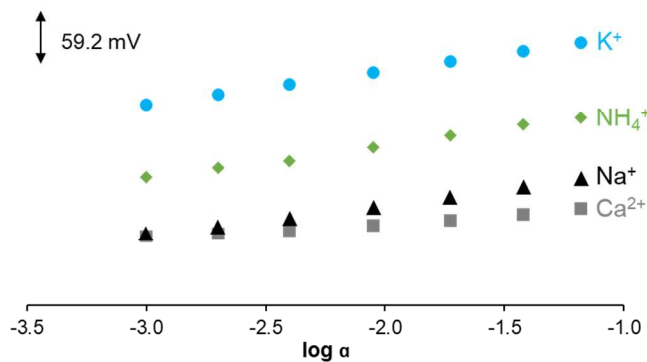


**Figure S13.** Potentiometric responses of glassy carbon electrodes coated with  $\text{Ni}_3\text{HHTP}_2$  and then covered with the  $\text{K}^+$ -ISM-I for various cations:  $\text{K}^+$  (blue circles),  $\text{NH}_4^+$  (green diamonds),  $\text{Na}^+$  (black triangles) and  $\text{Ca}^{2+}$  (grey squares).

## Selectivity Coefficients and Experimental Slopes Obtained for K<sup>+</sup> and NO<sub>3</sub><sup>-</sup>-ISEs

**Table S1.** Selectivity coefficients and experimental slopes obtained for K<sup>+</sup>-ISM-II containing Ni<sub>3</sub>HHTP<sub>2</sub> MOF as underlying conductive layer. (K<sup>+</sup> slope = 55.4 ± 0.8 mV).

Cation	Ca <sup>2+</sup>	Na <sup>+</sup>	NH <sub>4</sub> <sup>+</sup>
log K <sup>POT</sup>	-3.28 ± 0.02	-0.86 ± 0.10	-0.82 ± 0.05
Slope [mV]	24.3 ± 1.9	55.7 ± 1.7	54.4 ± 2.1

**Table S2.** Selectivity coefficients and experimental slopes obtained for NO<sub>3</sub><sup>-</sup>-ISM electrodes containing Ni<sub>3</sub>HHTP<sub>2</sub> MOF as underlying conductive layer (NO<sub>3</sub><sup>-</sup> slope = -56.3 ± 0.5 mV).

Cation	SO <sub>4</sub> <sup>2-</sup>	Cl <sup>-</sup>	Br <sup>-</sup>
log K <sup>POT</sup>	-3.15 ± 0.01	-1.82 ± 0.01	-0.48 ± 0.05
Slope [mV]	-28.7 ± 0.9	-55.2 ± 1.3	-55.0 ± 1.0

**Table S3.** Selectivity coefficients and experimental slopes obtained for K<sup>+</sup>-ISM-I containing Ni<sub>3</sub>HHTP<sub>2</sub> MOF as underlying conductive layer. (K<sup>+</sup> slope = 57.3 ± 0.2 mV).

Cation	Ca <sup>2+</sup>	Na <sup>+</sup>	NH <sub>4</sub> <sup>+</sup>
log K <sup>POT</sup>	-5.46 ± 0.09	-4.10 ± 0.01	-2.12 ± 0.05
Slope [mV]	25.1 ± 0.9	51.0 ± 0.5	55.9 ± 1.0



### Short-term Stability Measurement of $\text{NO}_3^-$ -ISM Electrodes with Drop-cast Layer of $\text{Ni}_3\text{HHTP}_2$ MOF.

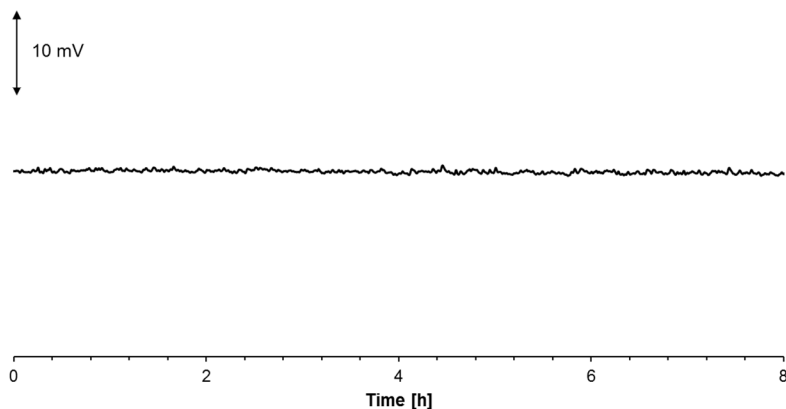


**Figure S14.** Short term stability of GCE/MOF/ $\text{NO}_3^-$ -ISM immersed in  $1.0 \times 10^{-3}$  M  $\text{NH}_4\text{NO}_3$ . Good potential stability with minimal drift was recorded for the electrodes with  $\text{Ni}_3\text{HHTP}_2$  used as ion-to-electron transducer. The electrodes were prepared according to the protocols described in the Experimental section.

### Long-term Stability Measurement of $\text{NO}_3^-$ -ISM Electrodes with Drop-cast Layer of $\text{Ni}_3\text{HHTP}_2$ MOF.

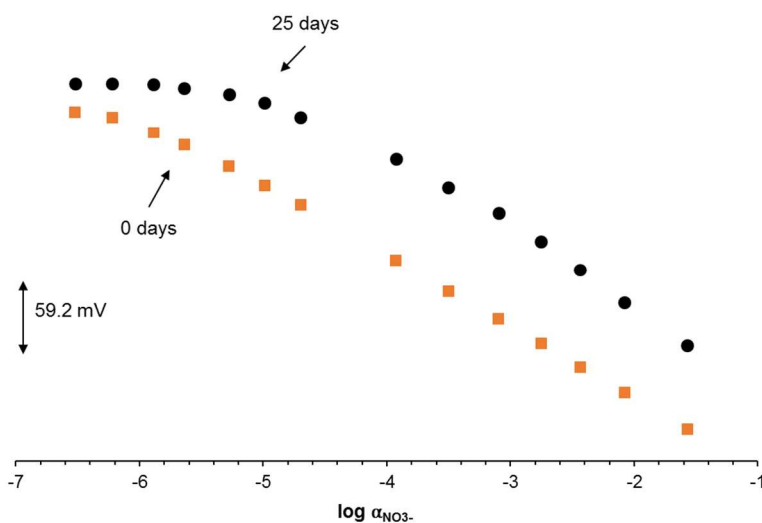


**Figure S15.** Long term stability of GCE/MOF/ $\text{NO}_3^-$ -ISM electrodes immersed in  $1.0 \times 10^{-3}$  M  $\text{NH}_4\text{NO}_3$ . Minimal change in standard potential ( $\sim 10 \text{ mV} \pm 3$ ) was recorded for the electrodes with  $\text{Ni}_3\text{HHTP}_2$  used as ion-to-electron transducer. The electrodes were stored in ultra-pure water for 25 days prior to the potentiometric experiments. The deterioration in the detection limits of these electrodes could attributed to leaching of membrane components from the polymeric matrix into the sample solution during storage. The electrodes were prepared according to the protocols described in the Experimental section.

### Light Stability of $K^+$ -ISM-II Electrodes with Drop-cast Layer of $Ni_3HHTP_2$ MOF.

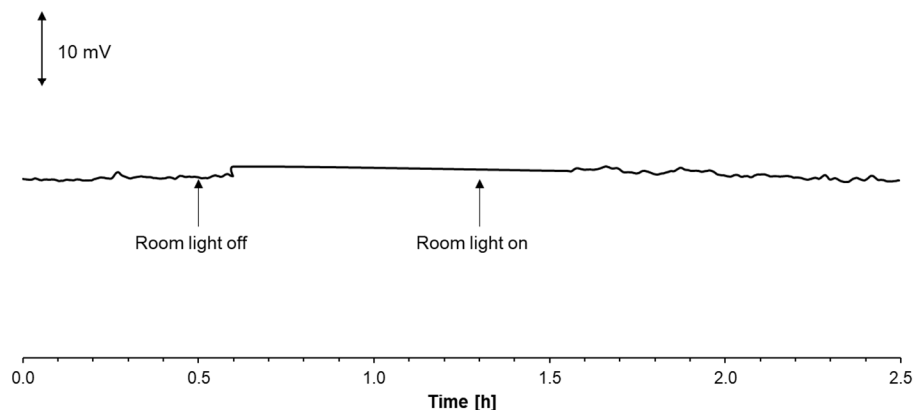


**Figure S16.** Light stability of GCE/MOF/ $K^+$ -ISM-II electrode immersed in  $1.0 \times 10^{-3}$  M KCl. Minimal potential drift was observed for the electrodes with  $Ni_3HHTP_2$  used as ion-to-electron transducer upon switching the room lights on and off.

### Powder X-ray Diffraction (pXRD) of $M_3HHTP_2$ MOFs After Potentiometric Measurements.

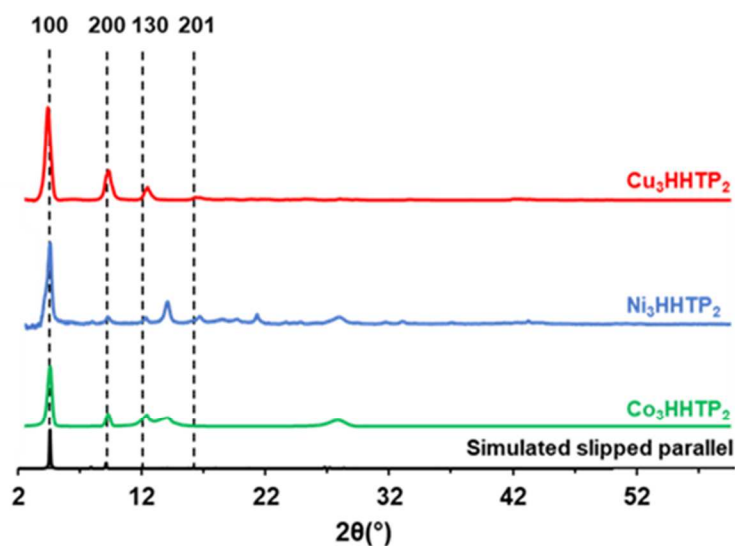


**Figure S17.** Experimental (colored) and simulated slipped parallel powder X-Ray Diffraction patterns without the presence of interpolated layer obtained for  $Cu_3HHTP_2$ ,  $Ni_3HHTP_2$  and  $Co_3HHTP_2$  MOFs after potentiometric measurements with  $K^+$ -ISM-II electrodes. The observed pXRD patterns of  $Cu_3HHTP_2$ ,  $Ni_3HHTP_2$ , and  $Co_3HHTP_2$  MOF matched those of bulk powder and are consistent with previous reports.<sup>1,2</sup> These findings indicate that the crystallinity of the MOF is retained both during and after analytical measurements.

### Contact Angle of Water on the Surface of Ni<sub>3</sub>HHTP<sub>2</sub> Coated Electrodes.

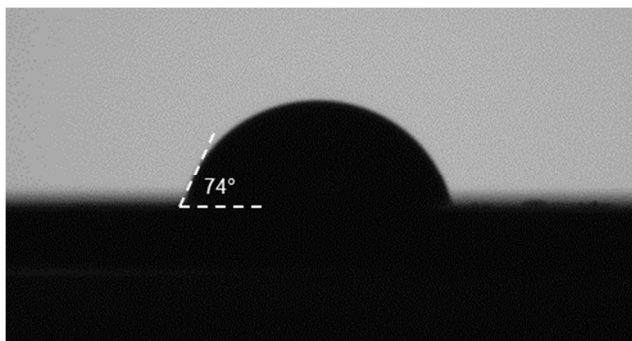


**Figure S18.** Contact angle image of 2  $\mu\text{L}$  of water placed on top of Ni<sub>3</sub>HHTP<sub>2</sub> coated glassy carbon electrode (GCE/Ni<sub>3</sub>HHTP<sub>2</sub> MOF).

### References

- (1) Smith, M. K.; Jensen, K. E.; Pivak, P. A.; Mirica, K. A. Direct Self-Assembly of Conductive Nanorods of Metal–Organic Frameworks into Chemiresistive Devices on Shrinkable Polymer Films. *Chem. Mater.* **2016**, *28*, 5264–5268.
- (2) Hmadeh, M.; Lu, Z.; Liu, Z.; Gandara, F.; Furukawa, H.; Wan, S.; Augustyn, V.; Chang, R.; Liao, L.; Zhou, F.; Perre, E.; Ozolins, V.; Suenaga, K.; Duan, X. F.; Dunn, B.; Yamamoto, Y.; Terasaki, O.; Yaghi, O. M. New Porous Crystals of Extended Metal-Catecholates. *Chem. Mater.* **2012**, *24*, 3511–3513.
- (3) Campbell, M. G.; Sheberla, D.; Liu, S. F.; Swager, T. M.; Dincă, M. Cu<sub>3</sub>(Hexaaminotriphenylene)<sub>2</sub>: An Electrically Conductive 2D Metal–Organic Framework for Chemiresistive Sensing. *Angew. Chem. Int. Ed.* **2015**, *54*, 4349–4352.
- (4) Sheberla, D.; Sun, L.; Blood-Forsythe, M. A.; Er, S.; Wade, C. R.; Brozek, C. K.; Aspuru-Guzik, A.; Dincă, M. High Electrical Conductivity in Ni<sub>3</sub>(2,3,6,7,10,11-Hexaaminotriphenylene)<sub>2</sub>, a Semiconducting Metal–Organic Graphene Analogue. *J. Am. Chem. Soc.* **2014**, *136*, 8859–8862.
- (5) Clough, A. J.; Yoo, J. W.; Mecklenburg, M. H.; Marinescu, S. C. Two-Dimensional Metal–Organic Surfaces for Efficient Hydrogen Evolution from Water. *J. Am. Chem. Soc.* **2015**, *137*, 118–121.
- (6) Chuang, T. J.; Brundle, C. R.; Rice, D. W. Interpretation of the X-Ray Photoemission Spectra of Cobalt Oxides and Cobalt Oxide Surfaces. *Surf. Sci.* **1976**, *59*, 413–429.
- (7) Biesinger, M. C.; Lau, L. W. M.; Gerson, A. R.; Smart, R. S. C. Resolving Surface Chemical States in XPS Analysis of First Row Transition Metals, Oxides and Hydroxides: Sc, Ti, V, Cu and Zn. *Appl. Surf. Sci.* **2010**, *257*, 887–898.
- (8) Biesinger, M. C.; Payne, B. P.; Grosvenor, A. P.; Lau, L. W. M.; Gerson, A. R.; Smart, R. S. C. Resolving Surface Chemical States in XPS Analysis of First Row Transition Metals, Oxides and Hydroxides: Cr, Mn, Fe, Co and Ni. *Appl. Surf. Sci.* **2011**, *257*, 2717–2730.
- (9) Grosvenor, A. P.; Biesinger, M. C.; Smart, R. S. C.; McIntyre, N. S. New Interpretations of XPS Spectra of Nickel Metal and Oxides. *Surf. Sci.* **2006**, *600*, 1771–1779.

- (10) Conway, B. E.; Pell, W. G. Double-Layer and Pseudocapacitance Types of Electrochemical Capacitors and Their Applications to the Development of Hybrid Devices. *J. Solid State Electrochem.* **2003**, *7*, 637–644.
- (11) Loera-Serna, S.; Oliver-Tolentino, M. A.; de Lourdes López-Núñez, M.; Santana-Cruz, A.; Guzmán-Vargas, A.; Cabrera-Sierra, R.; Beltrán, H. I.; Flores, J. Electrochemical Behavior of  $[\text{Cu}_3(\text{BTC})_2]$  Metal–organic Framework: The Effect of the Method of Synthesis. *J. Alloys Compd.* **2012**, *540*, 113–120.
- (12) Peng, Z.; Yi, X.; Liu, Z.; Shang, J.; Wang, D. Triphenylamine-Based Metal–Organic Frameworks as Cathode Materials in Lithium-Ion Batteries with Coexistence of Redox Active Sites, High Working Voltage, and High Rate Stability. *ACS Appl. Mater. Interfaces* **2016**, *8*, 14578–14585.
- (13) Naidek, K. P.; Zuconelli, C. R.; Cruz, O. M.; Ribeiro, R.; Winnischofer, S. M. B.; Winnischofer, H. Characterization of 2,3,6,7,10,11-Hexahydroxytriphenylene and Its Effects on Cell Viability in Human Cancer Cell Lines. *Biochem. Cell Biol.* **2016**, *94*, 205–211.